PERGAMON

Journal of Structural Geology 25 (2003) 1425–1444

JOURNAL OF STRUCTURAL GEOLOGY

www.elsevier.com/locate/jsg

Three-dimensional numerical modeling of lattice- and shape-preferred orientation of orthopyroxene porphyroclasts in peridotites

Takashi Sawaguchi[a], Kazuhiko Ishii[b,*]

[a]*Department of Earth Sciences, School of Education, Waseda University, Shinjiku, Tokyo 169-8050, Japan*
[b]*Division of Science Education, Osaka Kyoiku University, Kashiwara, Osaka 582-8582, Japan*

Received 3 March 2002; revised 18 November 2002; accepted 25 November 2002

Abstract

Orthopyroxene porphyroclasts in peridotite mylonites are elongated to variable extents depending on the crystallographic orientation. This paper presents a 3D numerical model of the development of lattice- and shape-preferred orientations of orthopyroxene porphyroclasts in a fine-grained olivine matrix for matrix deformations of simple shear, pure shear and uniaxial shortening. In this model, orthopyroxene grains are assumed to deform by dislocation glide on a unique slip system (100)[001] with additional rigid-body rotation. This rotation and deformation is determined so as to minimize the difference in displacement between the matrix and grains for an imposed incremental matrix deformation. The lattice- and shape-preferred orientations of orthopyroxene porphyroclasts in three mutually orthogonal sections of a peridotite mylonite sample are consistent with the simulation results for simple shear. The proposed model can be regarded as an extension of the rigid inclusion model to an anisotropically deformable model, and may represent a mechanism for the development of strong shape-preferred orientation with antithetic inclination from the shear direction. The proposed 3D model accounts for both lattice- and shape-preferred orientation, and may therefore be applicable to identifying finite strain geometry and the orientation of vorticity vectors independently in natural shear zones.

Keywords: Lattice-preferred orientation; Shape-preferred orientation; Orthopyroxene porphyroclast; Numerical model; Deformation of peridotite; Mica fish

1. Introduction

Orthopyroxene porphyroclasts in peridotite mylonites are elongated to variable extents depending on the crystallographic orientation (Darot and Boudier, 1975; Reuber et al., 1982; Suhr, 1993; Tubía, 1994; Sawaguchi and Takagi, 1997; Sawaguchi et al., 2001). Similar relationships are recognized in orthopyroxene porphyroclasts in granulite-facies basic mylonites (Dornbusch et al., 1994; Toyoshima, 1998; Hanmer, 2000). The present authors have recently simulated the development of lattice- and shape-preferred orientation (LPO and SPO) of orthopyroxene porphyroclasts embedded in a fine-gained olivine matrix using a 2D numerical model (Ishii and Sawaguchi, 2002). In the model, orthopyroxene grains are deformed by dislocation glide on a unique slip system (100)[001] (e.g. Mercier, 1985) and by rigid-body rotation. The magnitudes of this deformation and rotation are determined so as to minimize the difference in displacement between the matrix and grains for an imposed incremental matrix deformation. Therefore, favorably oriented grains for dislocation glide are highly deformed, whereas other grains undergo little deformation. In addition, grains with different shapes behave differently, even given identical crystallographic orientations.

Simulation results for initially circular grains show that glide-plane orientations (θ) of grains elongated to large aspect ratios (R) become separated into two groups during progressive matrix deformation ranging from simple shear to pure shear. In addition, the degree of asymmetry in the $R-\theta$ distribution increases with the degree of non-coaxiality of matrix deformation. In contrast, the grain long-axis orientations (ϕ) become concentrated around the maximum elongation axis of matrix deformation. A natural example from the Horoman peridotite complex, northern Japan, has an $R-\theta-\phi$ relation that is consistent with matrix deformation by progressive simple shear. Thus, the $R-\theta-\phi$

* Corresponding author. Present address: Department of Earth and Life Sciences, College of Integrated Arts and Sciences, Osaka Prefecture University, Sakai, Osaka 599-8531, Japan. Tel.: +81-72-254-9729; fax: +81-72-254-9932.
E-mail address: ishii@el.cias.osakafu-u.ac.jp (K. Ishii).

0191-8141/03/$ - see front matter © 2003 Elsevier Science Ltd. All rights reserved.
PII: S0191-8141(02)00199-2

relations of orthopyroxene porphyroclasts may be useful for the kinematical analysis of deformed peridotites.

In this paper, we extend our model to three dimensions and apply it to the same natural example. The effects of initial grain shape are also examined, and the results of the present model are discussed with respect to the results of various other models and natural examples. Such a 3D analysis has broader applicability than a 2D approach, which is only applicable to plane-strain deformations.

Various numerical models for the development of LPO have been proposed (e.g. Etchecopar, 1977; Lister et al., 1978; Lister and Paterson, 1979; Lister and Hobbs, 1980; Etchecopar and Vasseur, 1987; Molinari et al., 1987; Takeshita et al., 1990; Wenk et al., 1989, 1991; Zhang et al., 1994). These models have simulated the development of LPO of mono-mineralic (e.g. quartzite or dunite) or two-phase (e.g. olivine–orthopyroxene mixture) mineral aggregates. The present model simulates large grains embedded in a fine-grained matrix (i.e. orthopyroxene porphyroclasts in a fine-grained olivine matrix) and is able to trace the change in both crystallographic orientation and grain shape of orthopyroxene. In addition, this model considers the rigid-body rotation due to grain shape.

In contrast to models using the viscoplastic self-consistent theory (e.g. Molinari et al., 1987; Wenk et al., 1989, 1991; Takeshita et al., 1990) and models using the finite difference method (Zhang et al., 1994; Zhang and Wilson, 1997), the purely geometric nature of the present model does not account for rheology. The present model is therefore only applicable to the case when the critical resolved shear stress on a unique slip system is smaller than the matrix flow strength (Ishii and Sawaguchi, 2002). A model based on Eshelby's (1957) equations for ellipsoidal deformable inclusions may address this disadvantage. However, there are only a few studies on deformable inclusions (e.g. Eshelby, 1957; Bilby et al., 1975; Freeman, 1987) and no applications to natural examples. This area will need to be examined in the future.

Most theoretical models for the development of SPO are based on the rotational behavior of an isolated rigid particle in a deforming matrix. Jeffery (1922) derived the general equations for rotational behavior of a rigid ellipsoidal grain embedded in a slowly flowing incompressible viscous fluid. These equations have been solved both analytically and numerically for several conditions of grain shape and flow geometry (including 2D and 3D) and have been applied to the development of SPO (e.g. Jeffery, 1922; Gay, 1968; Reed and Tryggvason, 1974; Ghosh and Ramberg, 1976; Hinch and Leal, 1979; Freeman, 1985; Jezek et al., 1994, 1996; Masuda et al., 1995). Assuming rigid grains (i.e. no dislocation glide), the grain rotation indicated by our model is the same as Jeffery's (1922) equations within numerical error. Using a smaller increment of deformation and a larger number of points to define the grain shape will reduce this numerical error. Therefore, we believe that the principle of minimum difference in displacement between the grain and its matrix is a sufficient approximation of Jeffery's (1922) equations for a component of rigid-body rotation. From this point of view, the present model can be regarded as an extension of a rigid inclusion model to a deformable inclusion model.

2. A natural peridotite example

2.1. Analyzed sample and measurement

The sample used in analysis is the same as that used in the previous report (Ishii and Sawaguchi, 2002). It is a peridotite mylonite collected from the Horoman peridotite complex (Niida, 1974, 1975, 1984; Obata and Nagahara, 1987; Takahashi, 1991, 1992; Takazawa et al., 1992, 1996, 1999, 2000; Ozawa and Takahashi, 1995) in the Hidaka metamorphic belt (Komatsu et al., 1989; Osanai et al., 1992), Hokkaido, Japan. This sample is a harzburgite with the composition olivine + orthopyroxene + spinel ± clinopyroxene. Olivine grains are completely recrystallized into a polygonal fine-grained (≈230 μm) matrix with strong LPO, in which the olivine [100] point maximum is slightly oblique to the lineation (Ishii and Sawaguchi, 2002). Orthopyroxene porphyroclasts are variably elongated, defining structural elements such as foliation and lineation (Figs. 1 and 2).

Measurement of the LPO and SPO of orthopyroxene porphyroclasts was carried out for thin sections cut parallel to the lineation and normal to the foliation ($X'Z'$ plane), cut normal to the lineation ($Y'Z'$ plane), and cut parallel to the foliation ($X'Y'$ plane). Orientations of the crystallographic axes of porphyroclasts were measured using a petrographic microscope equipped with a U-stage. Aspect ratios (R) and long-axis orientations (ϕ) were also measured, and (100)-trace orientations (θ) of grains were reconstructed from the crystallographic orientations. A total of 102 grains from 12 $X'Z'$ sections, 38 grains from 5 $Y'Z'$ sections and 35 grains from 5 $X'Y'$ sections were examined.

Most orthopyroxene porphyroclasts are elliptical in all sections, and extremely elongated orthopyroxene grains become needle-like in the $X'Z'$ and $Y'Z'$ planes (Fig. 2a–c). The long axes of these grains range from 3 to 30 mm in $X'Z'$ plane, 1 to 7 mm in the $Y'Z'$ plane and 2 to 20 mm in the $X'Y'$ plane. The crystals exhibit wavy extinction and weakly

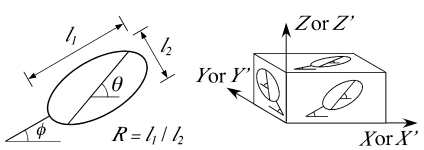

Fig. 1. Definition of geometrical parameters of a grain in sections. θ; orientation of (100)-plane trace, ϕ; long axis orientation, l_1, l_2; lengths of long and short axes, R; aspect ratio. The section is indicated by suffix, such as R_{XY}, θ_{XY} and ϕ_{XY}. For a natural grain, X' and Z' indicate lineation and foliation-normal of the peridotite. For a model grain, X and Z indicate long and short axes of the finite strain ellipsoid for matrix deformation.

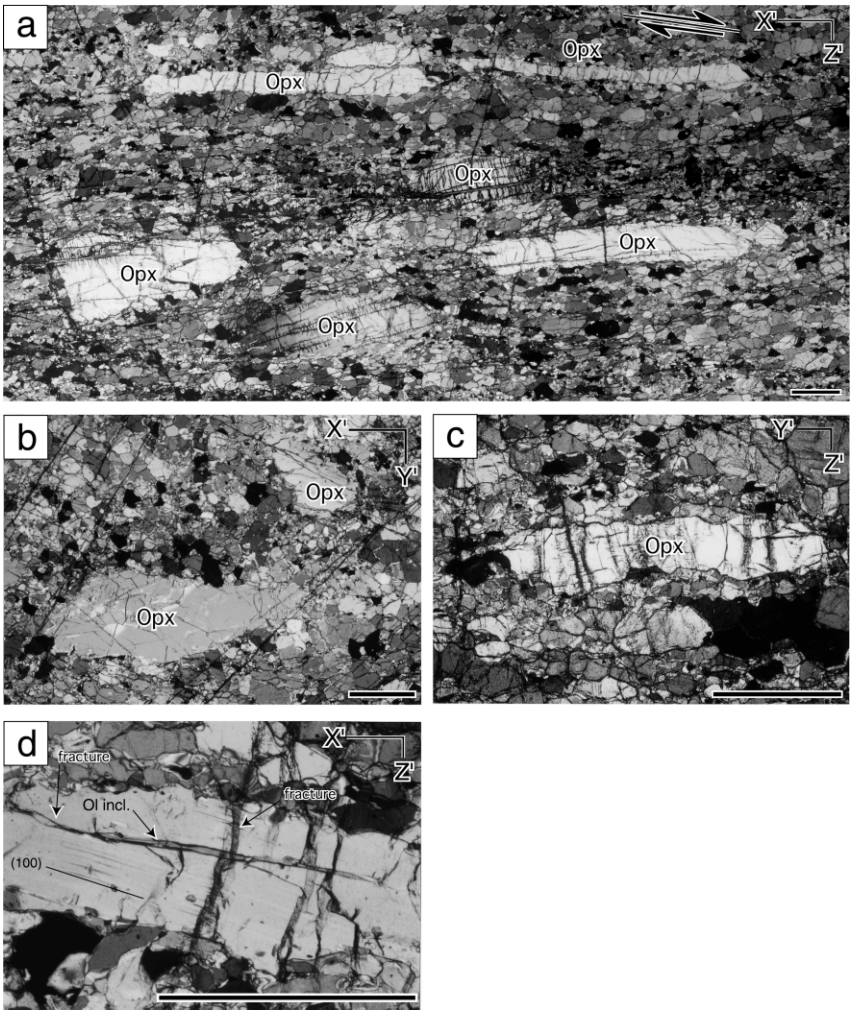

Fig. 2. Photomicrographs of orthopyroxene porphyroclasts (Opx) in fine-grained olivine matrix. Crossed polarizers. Scale bars are 1 mm. (a) $X'Z'$ plane. Coupled arrows indicate estimated shear direction. (b) $Y'Z'$ plane. (c) $X'Y'$ plane. (d) An elongated olivine inclusion in an orthopyroxene porphyroclast, which suggests shear along (100) slip plane of the host orthopyroxene porphyroclast. Brittle fracture extends from a tip of olivine inclusion almost parallel to (100) plane of the orthopyroxene. Fractures at high angle to the foliation are also visible.

curved (10°) exsolution lamellae of clinopyroxene along (100). Some grains contain sub-grain boundaries or kink band boundaries normal to (100) exsolution lamellae. The exsolution lamellae are slightly inclined with respect to the long axis of orthopyroxene porphyroclasts in the $X'Z'$ plane, and parallel to porphyroclasts in the $Y'Z'$ plane. The microstructure lacks heterogeneous deformation features such as shear bands, indicating that the present sample deformed homogeneously on the scale of a hand specimen.

In the $X'Z'$ and $X'Y'$ planes, no recrystallization was observed around the grain boundary of highly elongated orthopyroxene grains. In contrast, several grains with low aspect ratio exhibit evidence of recrystallization along grain boundaries; fine-grained aggregates composed of orthopyroxene and olivine extending parallel to the lineation from the grains. Therefore, the aspect ratio of low-aspect grains may be slightly affected by such grain boundary recrystallization. Some elongated orthopyroxene porphyroclasts contain elongated olivine inclusions with shape apparently governed by shear along the (100) slip plane of the host orthopyroxene porphyroclast (Fig. 2d).

Brittle fracture extends from a tip of olivine inclusion almost parallel to the (100) plane of the orthopyroxene (Fig. 2d) or radiating from the tip without displacement. There are also fractures at a high angle to the foliation in elongated orthopyroxene porphyroclasts, some of which extend into the olivine matrix (Fig. 2d). These fractures are thought to be formed after the plastic deformation of the orthopyroxene porphyroclast. Pairs of elongated orthopyroxene porphyroclasts with nearly identical crystallographic orientations are rarely arranged in a line parallel to the lineation on the $X'Z'$ plane, implying separation of the orthopyroxene porphyroclast into two pieces (i.e. microboudinage).

2.2. Results of measurements

Fig. 3 shows the LPO of 102 orthopyroxene porphyroclasts measured on $X'Z'$ thin sections. The [100] and [001]

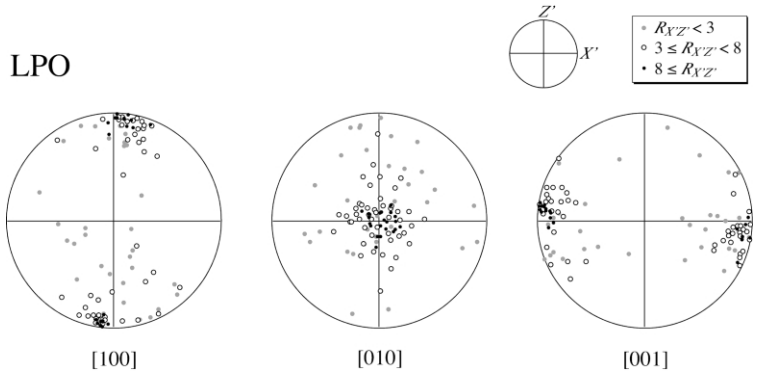

Fig. 3. LPO of orthopyroxene porphyroclasts in the Horoman peridotite mylonite.

orientations have small angles to the foliation-normal and lineation, respectively, and the [010] orientation has a point maximum parallel to the Y' axis. The crystallographic orientations of grains with larger $R_{X'Z'}$ values are more concentrated.

Fig. 4 shows the $R-\theta-\phi$ relations in the $X'Z'$, $Y'Z'$ and $X'Y'$ planes. In the $X'Z'$ plane (Fig. 4a), the maximum $R_{X'Z'}$ is 23.9. The $\phi_{X'Z'}$ values of most grains are within $\pm 20°$, whereas the $\theta_{X'Z'}$ values are more widely distributed. In addition, the $\theta_{X'Z'}$ values of grains of $3 < R_{X'Z'} < 6$ range from $-34°$ to 45°, while most grains of $6 < R_{X'Z'}$ have $\theta_{X'Z'}$ values ranging from $-20°$ to 0°. The $R_{X'Z'}-\theta_{X'Z'}$ distribution is therefore highly asymmetric. In the $\theta_{X'Z'}-\phi_{X'Z'}$ plot, grains with larger aspect ratios ($R_{X'Z'} \geqq 3$) can be divided into two groups of grains with $\theta_{X'Z'} > \phi_{X'Z'}$ and grains with $\theta_{X'Z'} < \phi_{X'Z'}$. All grains with $R_{X'Z'} \geqq 8$ have $\theta_{X'Z'} < \phi_{X'Z'}$, and the maximum $R_{X'Z'}$ in the $\theta_{X'Z'} > \phi_{X'Z'}$ group is 5.6. In the $Y'Z'$ plane (Fig. 4b), the maximum $R_{Y'Z'}$ is 8.0. The $\theta_{Y'Z'}$ and $\phi_{Y'Z'}$ of grains with large $R_{Y'Z'}$ values are concentrated around the foliation trace, while $\theta_{Y'Z'}$ and $\phi_{Y'Z'}$ of grains with small $R_{Y'Z'}$ values are more variable. In addition, $\theta_{Y'Z'}$ and $\phi_{Y'Z'}$ exhibit a positive correlation, reflecting the sub-parallelism of these orientations. In the $X'Y'$ plane (Fig. 4c), the maximum $R_{X'Y'}$ is 4.2. Although the $R_{X'Y'}-\theta_{X'Y'}-\phi_{X'Y'}$ distributions are dispersed, there is tendency that $\phi_{X'Y'}$ of grains with large $R_{X'Y'}$ values are concentrated around the lineation.

3. Numerical modeling

Extension of the previous 2D model (Ishii and Sawaguchi, 2002) to three dimensions is straightforward. Ellipsoidal grain shape is defined by regularly distributed points with positions $\boldsymbol{x}_i = \{x_i, y_i, z_i\}$ on the grain surface. Here, the displaced positions of these points after a deformation increment are dealt with. New positions for the matrix ($\boldsymbol{x}_i^{\mathrm{M}}$) and a grain ($\boldsymbol{x}_i^{\mathrm{G}}$) can be written by:

$$\boldsymbol{x}_i^{\mathrm{M}} = \mathbf{F}\mathbf{x}_i \tag{1}$$

and

$$\boldsymbol{x}_i^{\mathrm{G}} = \boldsymbol{W}^{\mathrm{t}}\boldsymbol{\Theta}\boldsymbol{\Gamma}\boldsymbol{\Theta}\mathbf{x}_i \tag{2}$$

where

$$\boldsymbol{F} = \begin{pmatrix} 1+a & 0 & \gamma \\ 0 & 1+b & 0 \\ 0 & 0 & 1-a-b \end{pmatrix},$$

$$\boldsymbol{W} = \begin{pmatrix} 1 & -\omega_3 & \omega_2 \\ \omega_3 & 1 & -\omega_1 \\ -\omega_2 & \omega_1 & 1 \end{pmatrix} \quad \text{and} \tag{3}$$

$$\boldsymbol{\Gamma} = \begin{pmatrix} 1 & 0 & 0 \\ 0 & 1 & 0 \\ \beta & 0 & 1 \end{pmatrix}$$

Here, $\boldsymbol{F}$ is a deformation gradient tensor for an incremental matrix deformation, $\boldsymbol{W}$ and $\boldsymbol{\Gamma}$ describe rigid rotation and dislocation glide on the (100)[001] slip system as components of grain deformation, $\boldsymbol{\Theta}$ is the transformation matrix, indicating the crystallographic orientation of the grain such that column vectors of $\boldsymbol{\Theta}$ correspond to the direction cosines of [100], [010] and [001] orientations. ${}^{\mathrm{t}}\boldsymbol{\Theta}$ is the transpose of $\boldsymbol{\Theta}$. Thus, for an imposed incremental matrix deformation (a, b, γ), the shear strain (β) and rotation (ω_1, ω_2, ω_3) of grains are determined so as to minimize the following expression:

$$\sum_i \sqrt{\left(x_i^{\mathrm{G}} - x_i^{\mathrm{M}}\right)^2 + \left(y_i^{\mathrm{G}} - y_i^{\mathrm{M}}\right)^2 + \left(z_i^{\mathrm{G}} - z_i^{\mathrm{M}}\right)^2} \tag{4}$$

New grain positions (Eq. (2)) and a new crystallographic orientation ($\boldsymbol{W}\cdot\boldsymbol{\Theta}$) are determined from these ω_1, ω_2, ω_3 and β, and the next deformation increment is then computed.

The progressive deformation of 300 initially spherical grains with nearly random initial crystallographic orientations was computed for matrix deformations of simple shear, pure shear, uniaxial shortening and combinations thereof. The components of incremental matrix deformations are assumed to be constant during the deformation.

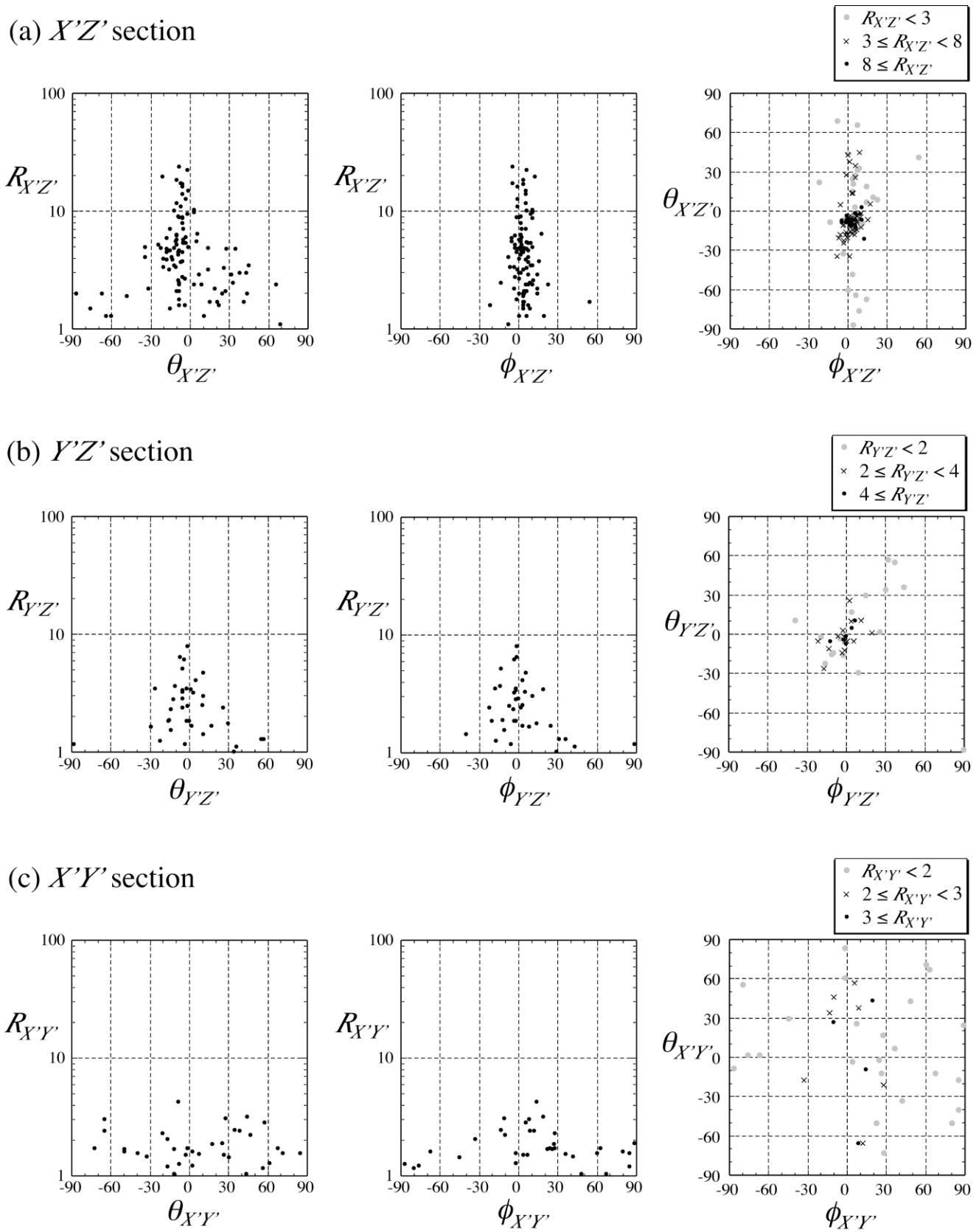

Fig. 4. $R-\theta-\phi$ relations of orthopyroxene porphyroclasts in the Horoman peridotite mylonite. (a) $X'Z'$ section. (b) $Y'Z'$ section. (c) $X'Y'$ section.

4. Results of numerical simulation

Deformation of a model grain is affected by three factors; geometry of matrix deformation, lattice orientation, and grain shape. For example, Fig. 5 shows the deformation and rotation of several grains with different lattice orientations in a matrix deforming by simple shear. Grain A is deformed only by simple shear without any additional rigid-body rotation because its slip plane and slip direction are parallel to the shear plane and the shear direction of matrix deformation, respectively. Grain C is deformed with a shear sense opposite to the matrix deformation (antithetic shear) with an additional clockwise rigid-body rotation. Grain B rotates clockwise with little deformation because its orientation is unfavorable for dislocation glide. However, during progressive matrix deformation, grain B rotates to an orientation favorable for dislocation glide, after which it is elongated. Grains D and E only rotate and cannot be deformed permanently. The authors previously (Ishii and Sawaguchi, 2002) described in detail the rotational and deformational behavior of 2D grains. The results of that study will also be helpful in understanding the behavior of 3D grains.

4.1. Simple shear

Fig. 6 shows the LPO and SPO of 300 grains in a matrix deforming by progressive simple shear ($a = b = 0$, $\gamma = 0.02$). Note that X, Y and Z in the simulation indicate the principal axes of the finite strain ellipsoid for matrix deformation ($X \geqq Y \geqq Z$). Grains with larger R_{XZ} values display stronger LPO, while nearly spherical grains exhibit weak LPO. The [010] orientations of grains with large R_{XZ} value have a point maximum near the Y axis. In contrast, the [001] orientations of grains with $R_{XZ} > 3$ have two maxima that are slightly oblique to the X axis. One of these maxima is parallel to the shear direction of matrix deformation and is more strongly concentrated than the other maximum. Similarly, the [100] orientations of grains with $R_{XZ} > 3$ have two maxima that are slightly oblique to the Z axis. Therefore, the overall LPO has monoclinic symmetry.

The orientations of long, intermediate and short axes of grains with large R_{XZ} values have point maxima parallel to the X, Y and Z axes, respectively. Therefore, the overall SPO has nearly orthorhombic symmetry with respect to finite strain coordinates.

Fig. 7 shows the $R-\phi-\theta$ relations in the XZ, XY and YZ sections for matrix deformation by simple shear. In the XZ section (Fig. 7a), grains are separated into two groups of $\theta_{XZ} < \phi_{XZ}$ and $\theta_{XZ} > \phi_{XZ}$. These two groups correspond to the two maxima in the LPOs of [100] and [001] (Fig. 6a). Grains with large R_{XZ} values in the $\theta_{XZ} < \phi_{XZ}$ group have θ_{XZ} orientations nearly parallel to the shear plane of matrix deformation. The maximum R_{XZ} value in the $\theta_{XZ} < \phi_{XZ}$ group is larger than that in the $\theta_{XZ} > \phi_{XZ}$ group. Grains with large R_{XZ} values in both groups have ϕ_{XZ} orientations nearly parallel to the X axis. These $R_{XZ}-\phi_{XZ}-\theta_{XZ}$ relations are basically the same as the results of the 2D simulation (Ishii and Sawaguchi, 2002).

In the YZ section (Fig. 7b), the grain with maximum R_{YZ} has ϕ_{YZ} and θ_{YZ} orientations parallel to the Y axis, whereas grains with smaller R_{YZ} values exhibit a wide range of ϕ_{YZ} and θ_{YZ} values. The values of ϕ_{YZ} and θ_{YZ} exhibit a positive correlation, indicating that the two orientations are sub-parallel. In the XY section (Fig. 7c), grains with large R_{XY} values have ϕ_{XY} orientations concentrated around the X axis and exhibit a wide range of θ_{XY} values. But there are no grains with $R_{XY} > 2$ and $\theta_{XY} \approx 0$. The $\phi_{XY}-\theta_{XY}$ graph includes a diagonal blank space, indicating that the ϕ_{XY} and θ_{XY} orientations are not parallel.

4.2. Pure shear

For matrix deformation by progressive pure shear ($a = 0.01$, $b = 0$, $\gamma = 0$), LPO and SPO exhibit orthorhombic symmetry (Fig. 8). The [100] and [001] orientations of grains with large R_{XZ} values have two maxima at some angle away from the Z axis and X axis, respectively, while the

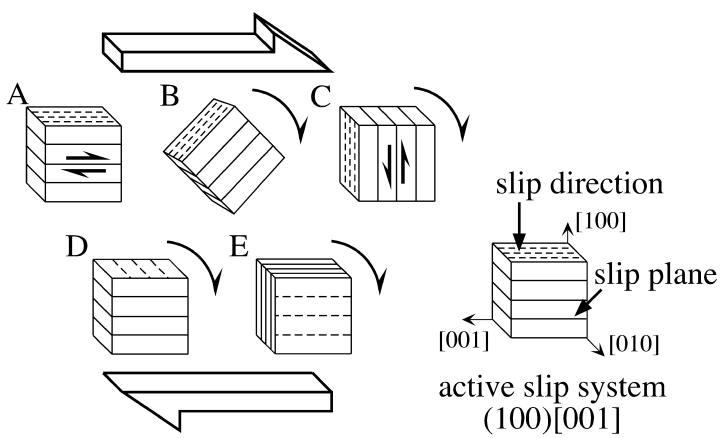

Fig. 5. Deformation (solid coupled arrows) and rotation (curved arrows) of spherical model grains with different lattice orientations in a matrix deforming by simple shear (open coupled arrows). Grain shapes are shown as cubic for the sake of clear presentation of the orientation of active slip system (100)[001].

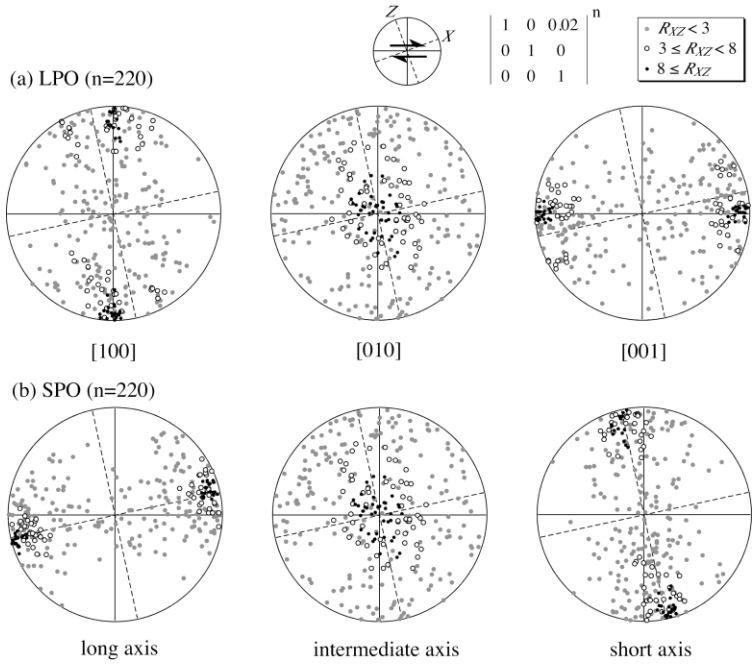

Fig. 6. LPO (a) and SPO (b) of grains in a matrix deforming by progressive simple shear after deformation increments (n) of 220. The shear-plane orientation, sense of shear (coupled arrows) and X and Z axes orientation for a matrix deformation are shown in an inset. Axial ratio of a finite strain ellipsoid for matrix deformation is $X{:}Y{:}Z = 4.62{:}1{:}0.22$.

[010] orientations of similar grains have a point maximum parallel to the Y axis. The orientations of the long, intermediate and short axes of grains with large R_{XZ} values have point maxima parallel to the X, Y and Z axes. Fig. 9 shows the $R-\phi-\theta$ relations in three sections for the pure shear matrix deformation. $R-\phi-\theta$ relations are similar to those for a matrix deformation by simple shear. However, all $R-\phi-\theta$ relations are symmetrical with respect to the X, Y and Z axes.

4.3. Uniaxial shortening

The LPO and SPO for uniaxial shortening ($a = b = 0.01$, $\gamma = 0$) exhibit uniaxial symmetry (Fig. 10). The [100] and [001] orientations form ca. 15° and 75° small-circle distributions about the Z axis, while the [010] orientations have a diffuse girdle distribution parallel to the XY plane. The orientations of long and intermediate axes of grains show girdle distributions parallel to the XY plane and those of the short axes have a point maximum parallel to the Z axis. The LPO and SPO for grains with large R_{XZ} values do not have girdle or small-circle distributions, instead having one or two point maxima. However, the overall fabric symmetry is axial, not orthorhombic. For example, grains with long-axis orientation parallel to the Y axis or X axis have the same 3D grain shape, although the aspect ratios in the XZ section (R_{XZ}) are different.

Fig. 11 shows the $R-\phi-\theta$ relation in the XZ and XY sections for uniaxial shortening. The $R_{XZ}-\theta_{XZ}$ distribution has two maxima, indicating the sectioning effect through the 3D fabric with axial symmetry. In the XY section, the ϕ_{XY} and θ_{XY} distributions are nearly uniform. However, the angles between ϕ_{XY} and θ_{XY} are larger than 30°, indicated by the diagonal blank space in the $\phi_{XY}-\theta_{XY}$ graph.

4.4. General shear

The results for the three cases of matrix deformation described above can be considered as end members of LPO and SPO development for general shear deformation. The LPO and $R-\phi-\theta$ relation for a combination of simple shear and pure shear ($a = 0.01$, $b = 0$, $\gamma = 0.04$; Fig. 12) are nearly the same as that of simple shear (Figs. 6 and 7). However, the addition of a pure shear component reduces the difference in maximum R_{XZ} values between the $\theta_{XZ} < \phi_{XZ}$ and $\theta_{XZ} > \phi_{XZ}$ groups (compare Figs. 7a and 12b; see also Ishii and Sawaguchi, 2002).

In the case shown in Fig. 13, the elongation axis of the pure shear component is perpendicular to the shear direction of the simple shear component ($a = 0$, $b = 0.01$, $\gamma = 0.05$). The LPO exhibits monoclinic symmetry (Fig. 13a). The [001] orientations of grains with $R_{XZ} \geqq 3$ form part of ca. 80° small-circle girdle about the shear-plane normal. The [100] orientations have a point maximum slightly oblique to the shear-plane normal, and the [010] orientation fall in a diffuse girdle pattern normal to the [100] point maximum. The $R-\phi$ distributions in three sections indicate that grains are elongated in all directions within the XY plane (Fig. 13b–d). This is a reflection of the nearly oblate geometry of the finite strain ellipsoid for this matrix deformation ($X{:}Y{:}Z = 3.79{:}3.65{:}0.07$). In contrast, the $R_{XZ}-\theta_{XZ}$ distribution shows clear asymmetry.

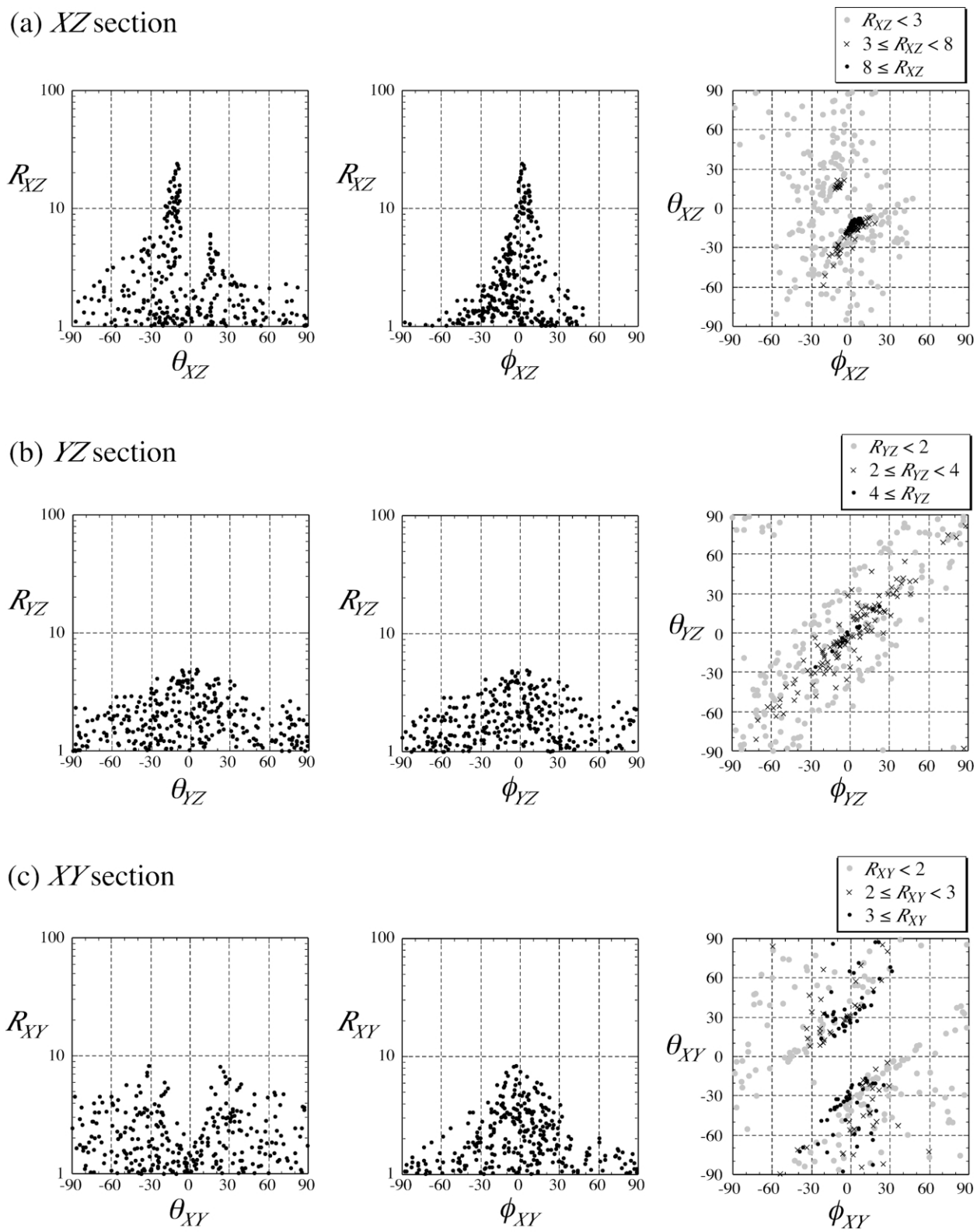

Fig. 7. $R-\theta-\phi$ relations in XZ section (a), YZ section (b) and XY section (c) after 220 deformation increments by simple shear.

For a combination of simple shear and uniaxial shortening ($a = b = 0.01$, $\gamma = 0.05$), the [100] and [001] orientations of grains with large R_{XZ} values have two maxima with different concentrations, reflecting a component of simple shear (Fig. 14a). The [100] and [001] orientations of grains with small R_{XZ} values form small-circle distributions, reflecting a component of uniaxial shortening. The strong, moderate and weak development of

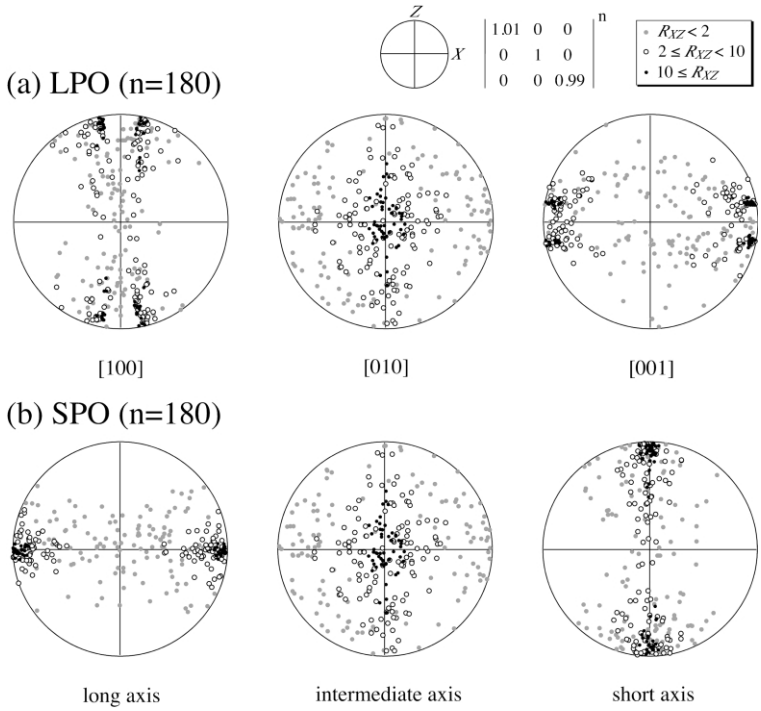

Fig. 8. LPO (a) and SPO (b) of grains in a matrix deforming by progressive pure shear after deformation increments (n) of 180. Axial ratio of a finite strain ellipsoid for matrix deformation is $X{:}Y{:}Z = 6.00{:}1{:}0.16$.

SPO in the XZ, YZ and XY sections ($R-\phi$ distributions in Fig. 14b–d), respectively, reflect the geometry of the finite strain ellipsoid for this matrix deformation ($X{:}Y{:}Z = 4.03{:}2.22{:}0.11$).

5. Discussion

5.1. Comparison with natural example

The simulation results show that the LPO and SPO of orthopyroxene porphyroclasts have the same symmetry as the matrix deformation: fabrics with axial (uniaxial shortening), orthorhombic (pure shear) or monoclinic symmetry (simple shear). However, the SPO for simple shear matrix deformation has nearly orthorhombic symmetry. It is very difficult to measure the 3D SPO directly from a natural example. However, it is possible to compare the simulation results with a natural example by comparing the $R-\theta-\phi$ data distributions in sections with clear orientations.

As foliation ($X'Y'$ plane) and lineation (X' axis) in the present natural sample are defined by the SPO of orthopyroxene porphyroclasts (Figs. 2 and 4) and all of the simulation results indicate an SPO parallel to the finite strain axes of matrix deformation (X, Y and Z axes), the simulation results can be compared with a natural example by regarding the X', Y' and Z' axes as the finite strain axes of matrix deformation. The LPO and $R-\theta-\phi$ distributions of orthopyroxene porphyroclasts in the present natural sample (Figs. 3 and 4) are almost identical to the simulation result for progressive simple shear after 220 deformation increments (Figs. 6 and 7). The shear plane and shear direction of the natural example are estimated to be a plane normal to [100] maximum and a direction of [001] maximum, respectively.

However, there are several differences between the two series of results. Most notably, the simulation yields a smaller maximum R_{YZ} and larger maximum R_{XY} than the natural example. Calculations for various matrix deformations show that these differences cannot be reduced by the addition of a small pure shear or uniaxial shortening component (a and/or b in Eq. (3)) to the simple shear (compare Figs. 12–14 with Fig. 7). The LPO and $R-\theta-\phi$ distributions for matrix deformation with a/γ or b/γ values larger than 0.1 are also clearly different from those of the natural example (compare [001] orientations in Figs. 13 and 14 with those in Fig. 3). The differences in maximum R_{YZ} and R_{XY} will be discussed later.

There have been no previous reports on the data sets including LPO and $R-\theta-\phi$ distributions for orthopyroxene porphyroclasts in mylonitic rocks. Therefore, observations of the present natural example are the only data on which to base a concrete discussion of the simulation results. However, Dornbusch et al. (1994) analyzed granulite-facies metabasic mylonites from the Ivrea Zone of the Southern Alps in Italy. Those mylonites also include variably elongated orthopyroxene porphyroclasts within recrystallized fine-grained plagioclase. Although Dornbusch et al. (1994) did not show the $R_{X'Z'}-\theta_{X'Z'}$ or $\phi_{X'Z'}-\theta_{X'Z'}$ distributions, the reported LPO and $R_{X'Z'}-\phi_{X'Z'}$ distributions of

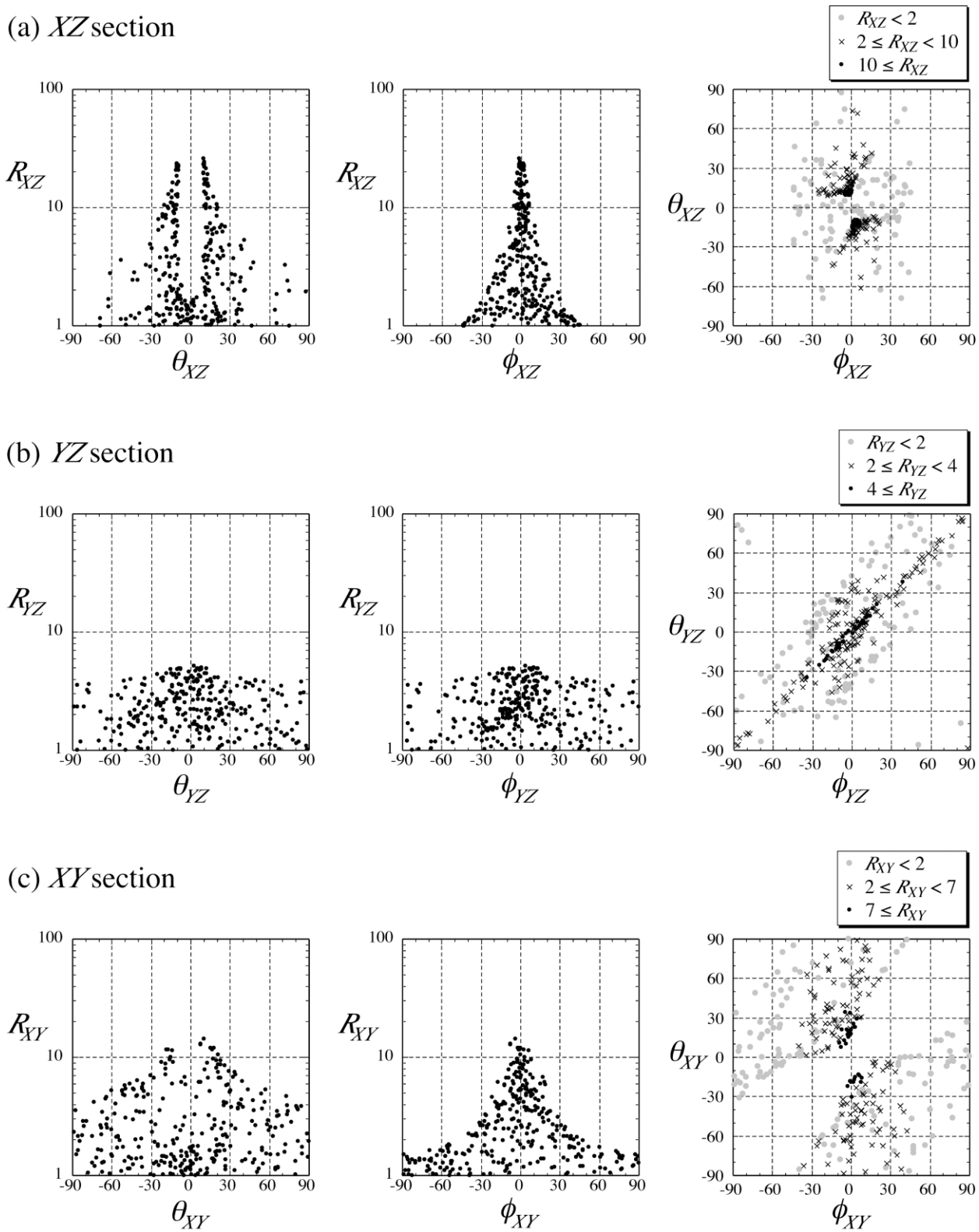

Fig. 9. $R-\theta-\phi$ relations in XZ section (a), YZ section (b) and XY section (c) after 180 deformation increments by pure shear.

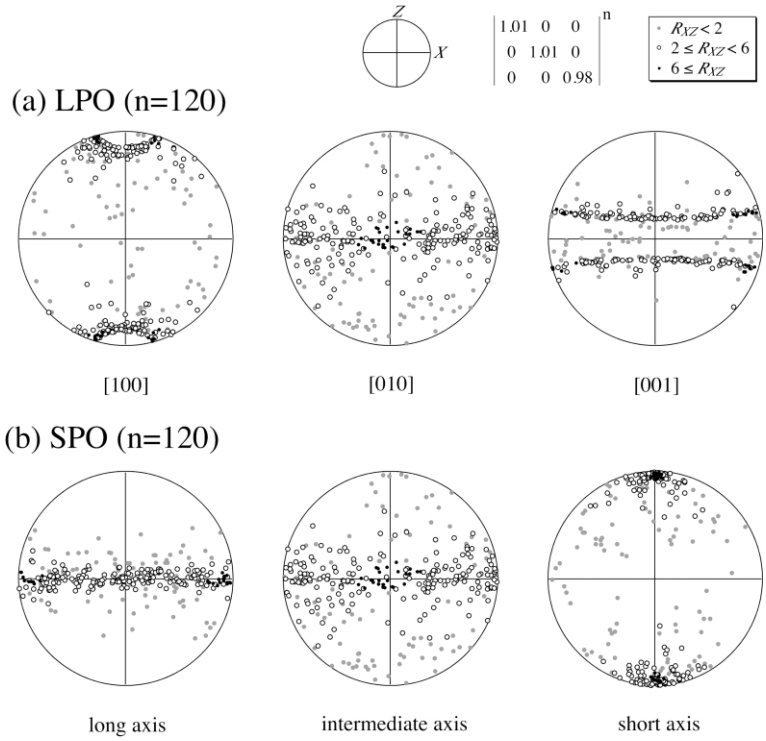

Fig. 10. LPO (a) and SPO (b) of grains in a matrix deforming by progressive uniaxial shortening after deformation increments (n) of 120. Axial ratio of a finite strain ellipsoid for matrix deformation is $X{:}Y{:}Z = 3.30{:}3.30{:}0.09$.

orthopyroxene porphyroclasts is consistent with a present simulation result for matrix deformation by simple shear.

5.2. Effect of initial grain shape

As there are differences in maximum R_{YZ} and R_{XY} values between the natural example and the simulation for initially spherical grains, the effect of non-spherical initial grain shapes were examined by calculations for initially ellipsoidal grains with axes parallel to the crystallographic axes [100], [010] and [001]. The result most consistent with the natural example was obtained from the initial grain shape of $d_1{:}d_2{:}d_3 = 1{:}2{:}1.4$, where d_1, d_2 and d_3 indicate the grain diameters parallel to the [100], [010] and [001] directions, respectively (Figs. 15 and 16). In general, a larger maximum R_{YZ} and smaller maximum R_{XY} result from initial grain shapes with larger d_2/d_1 ratio. In addition, larger d_3/d_1 tends to result in greater asymmetry in the R_{XZ}–θ_{XZ} distribution (i.e. a larger difference in maximum R_{XZ} values between the $\theta_{XZ} > \phi_{XZ}$ and $\theta_{XZ} < \phi_{XZ}$ groups) for matrix deformation by simple shear.

Although it is difficult to fully understand the combined effects of various matrix deformation and initial grain shapes, it can be confirmed that initial grain shapes of $0.5 < d_i/d_j < 2$ ($i, j = 1, 2, 3$) do not significantly affect the LPO.

5.3. Mica fish

Mica fish are porphyroclasts composed of muscovite or biotite with parallelogram or lenticular shapes occurring within quartz-rich mylonites (Lister and Snoke, 1984; Passchier and Trouw, 1996). Lister and Snoke (1984) described that the (001) cleavage of mica fish is either tilted (30–40°) back against the sense of shear or sub-parallel to the shear plane (C-plane). Judging from the microphotographs (see also Passchier and Trouw, 1996), the long axis orientation of mica fish range from 30° back against the sense of shear to parallel to the shear plane such that the long axis orientation with respect to the (001) cleavage varies from −20° to 20°. In addition, Lister and Snoke (1984) have shown that elongated mica fish (aspect ratio larger than 20) with (001) plane parallel to the C-planes are also common. The R–ϕ distributions of mica fish from two localities were reported by ten Grotenhuis et al. (2002), who showed that the long axis orientation of mica fish ranged from 30° back against the sense of shear to parallel to the shear plane, with aspect ratios of 2–16. Microphotographs indicated that the mica fish have similar (001) orientations to those described by Lister and Snoke (1984). These variations in mica fish geometry are similar to those of the model grains within a simple-shearing matrix.

However, the microstructures of mica fish reveal formation mechanisms of recrystallization and microfaulting of mica porphyroclasts as well as slip on the basal plane and rigid body rotation (Lister and Snoke, 1984; Passchier

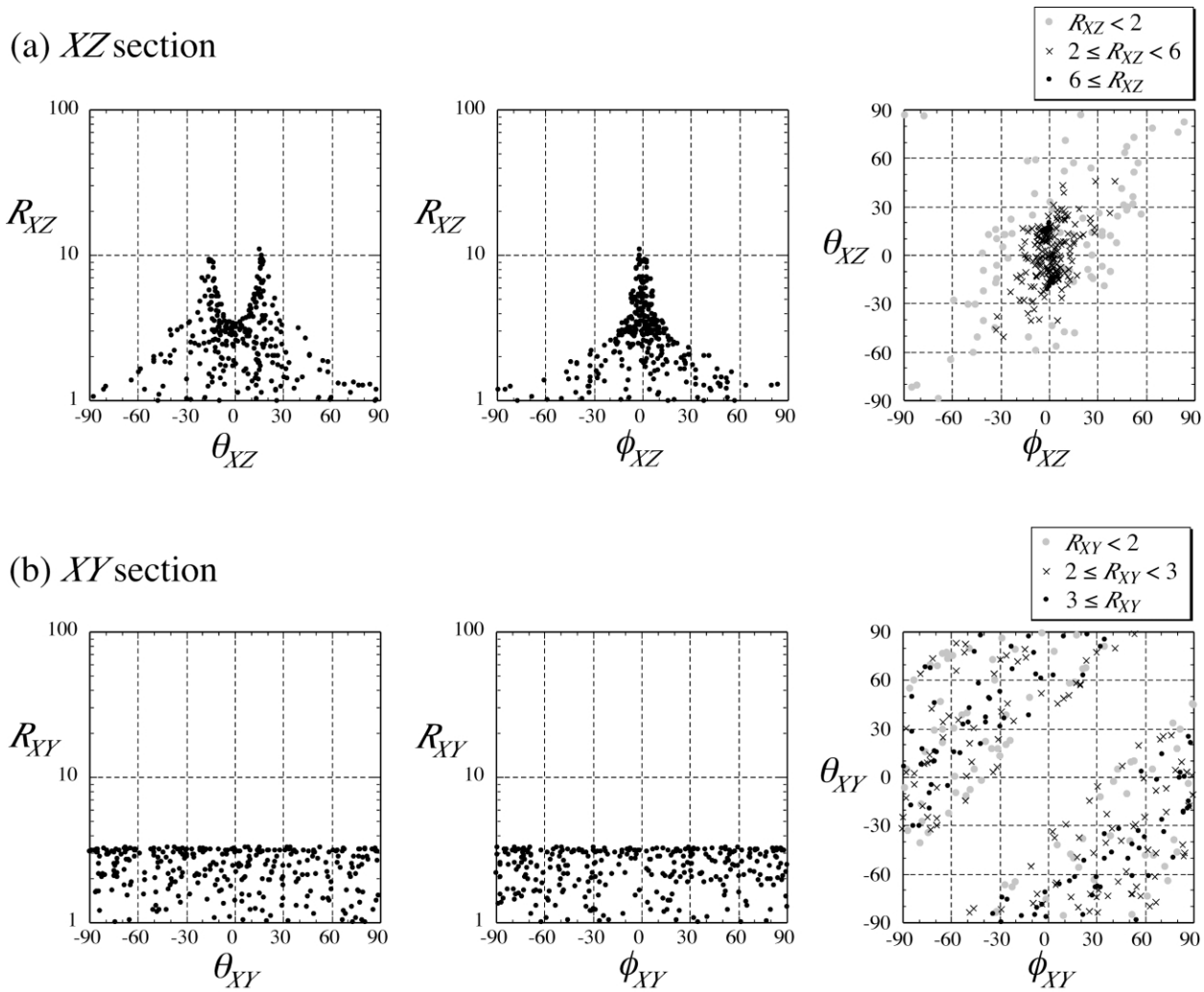

Fig. 11. $R-\theta-\phi$ relations in XZ section (a) and XY section (b) after 120 deformation increments by uniaxial shortening.

and Trouw, 1996). Microfaults are parallel or oblique to the (001) cleavage, and have antithetic or synthetic relationships with bulk shear sense depending on the orientation with respect to the bulk shear plane (fig. 5 of Lister and Snoke, 1984). Most mica fish have trails of small fragments or recrystallized grains extending from tips. Since the $R-\phi-\theta$ relations of mica fish can be affected by these microfaulting and recrystallization processes, detailed studies on the $R-\phi-\theta$ relations for mica fish are required before applying the present model.

5.4. SPO antithetically inclined from the shear direction

Based on the Jeffery's (1922) equations, a rigid ellipsoidal grain should continuously rotate in a linear-viscous matrix undergoing simple shear, and will therefore not develop a stable orientation (e.g. Freeman, 1985; Jezek et al., 1994; Masuda et al., 1995). However, many natural mylonitic rocks exhibit very strong SPO of porphyroclasts with long axes inclined antithetically to the shear direction. This is considered to be more consistent with a stable end orientation than the transient fabrics predicted by the theory (Pennacchioni et al., 2001; ten Grotenhuis et al., 2002; Mancktelow et al., 2002).

Jeffery's (1922) equations predict that an additional pure shear component in matrix flow results in a stable end orientation for grains above a critical aspect ratio (Ghosh and Ramberg, 1976; Passchier, 1987; Masuda et al., 1995). In this case, stable orientation with regard to the shear sense is synthetic for thinning shear zones and antithetic for thickening shear zones.

The non-Newtonian rheology of matrices (Ildefonse and Mancktelow, 1993; ten Grotenhuis et al., 2002), particle interaction in multiparticle systems (Ildefonse et al., 1992a, b; Tikoff and Teyssier, 1994; Arbaret et al., 1996) and slip at particle–matrix interfaces (Ildefonse and Mancktelow, 1993; Marques and Coelho, 2001; Mancktelow et al., 2002) also affects the development of SPO. Particle interaction will stabilize shape fabric toward an antithetic orientation with respect to the shear plane, but the intensity of such a fabric is very weak (Ildefonse et al., 1992a,b; Arbaret et al., 1996).

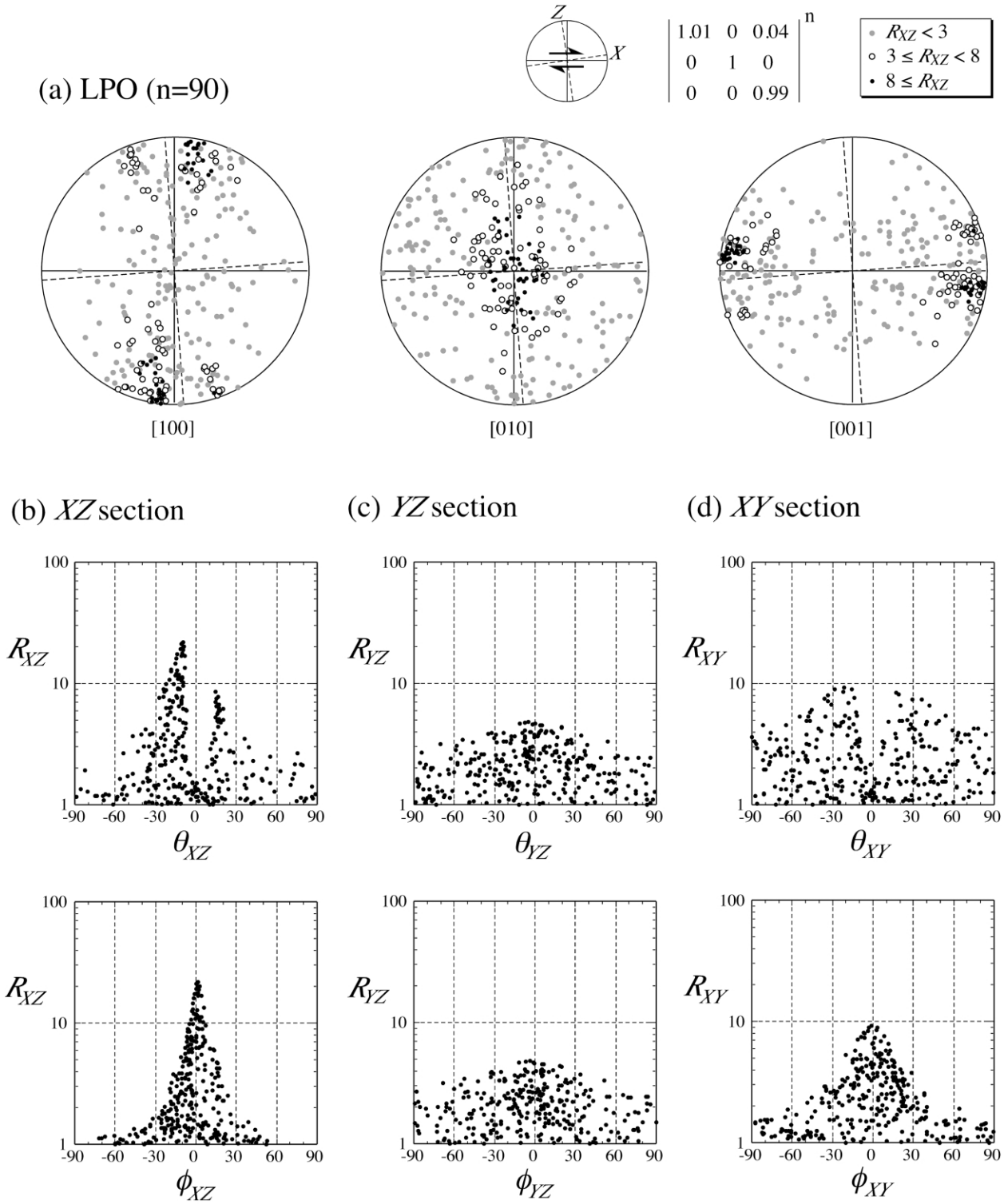

Fig. 12. LPO (a) and $R-\theta-\phi$ relations in three sections ((b)–(d)) for a matrix deformation by a combination of progressive simple shear and pure shear. The elongation axis of a pure shear component is parallel to the shear direction of a simple shear component (coupled arrows in an inset). Axial ratio of a finite strain ellipsoid for matrix deformation is $X{:}Y{:}Z = 4.78{:}1{:}0.21$.

From analog experiments of simple shear and combinations of pure and simple shear using Mohr–Coulomb type material, ten Grotenhuis et al. (2002) have shown that rigid elongate parallelogram-shaped inclusions have stable end orientations inclined antithetically from the shear plane. Among the several conditions of non-coaxiality, the results of simple shear experiments fit very well with the SPO of natural mica and tourmaline fish. The results also suggest

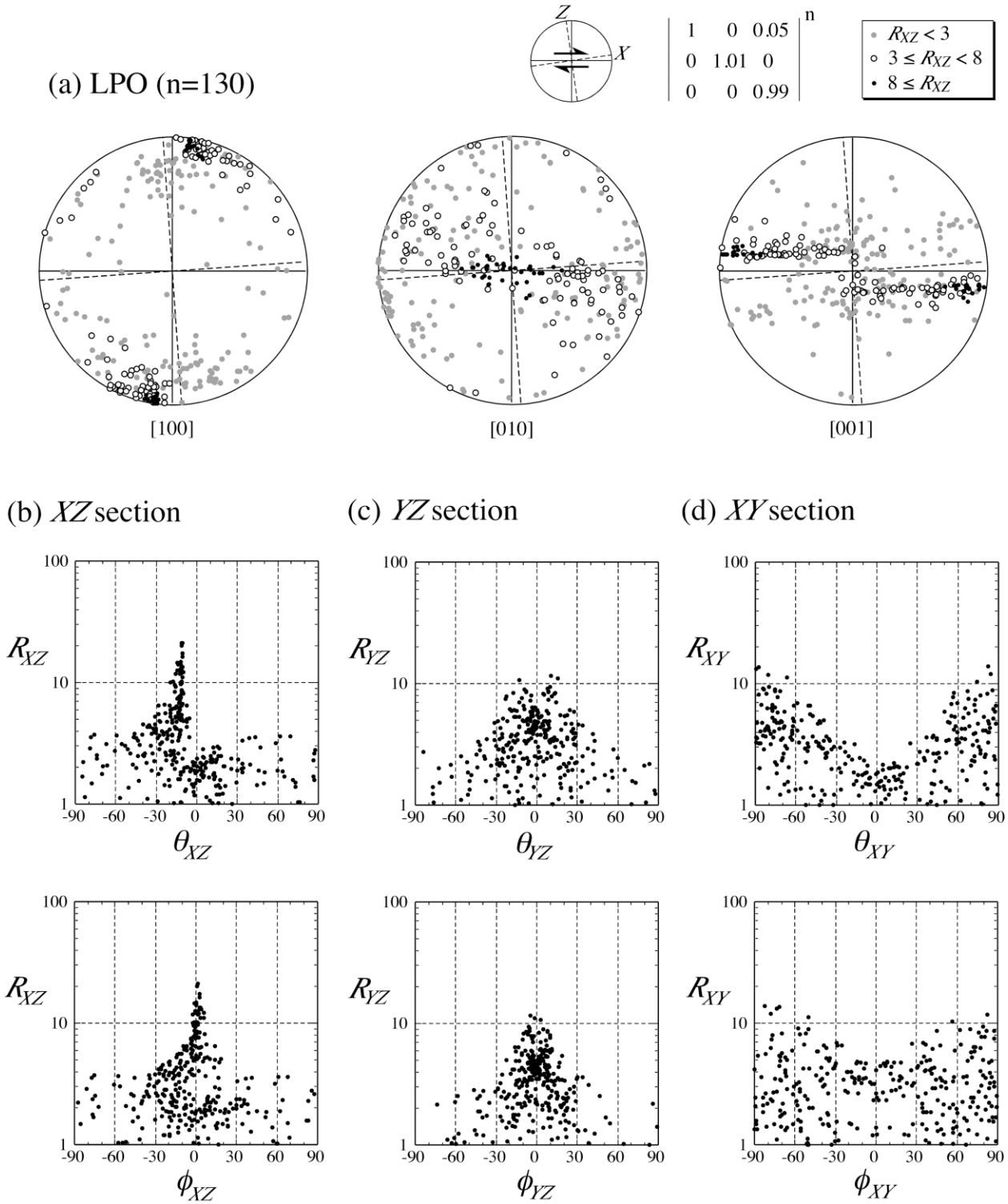

Fig. 13. LPO (a) and $R-\theta-\phi$ relations in three sections ((b)–(d)) for a matrix deformation by a combination of progressive simple shear and pure shear. The elongation axis of a pure shear component is normal to the page and is perpendicular to the shear direction of a simple shear component (coupled arrows in an inset). Axial ratio of a finite strain ellipsoid for matrix deformation is $X{:}Y{:}Z = 3.79{:}3.65{:}0.07$.

that orientation of the object is determined by the orientation of small-scale shear bands. Mancktelow et al. (2002) performed analog experiments at very high simple shear strain using linear-viscous material and investigated the rotational behavior of rigid elongate inclusions with elliptical and parallelogram shapes under conditions of coherent and slipping inclusion–matrix interfaces. Interface slip causes a dramatic reduction in the rotation rate of

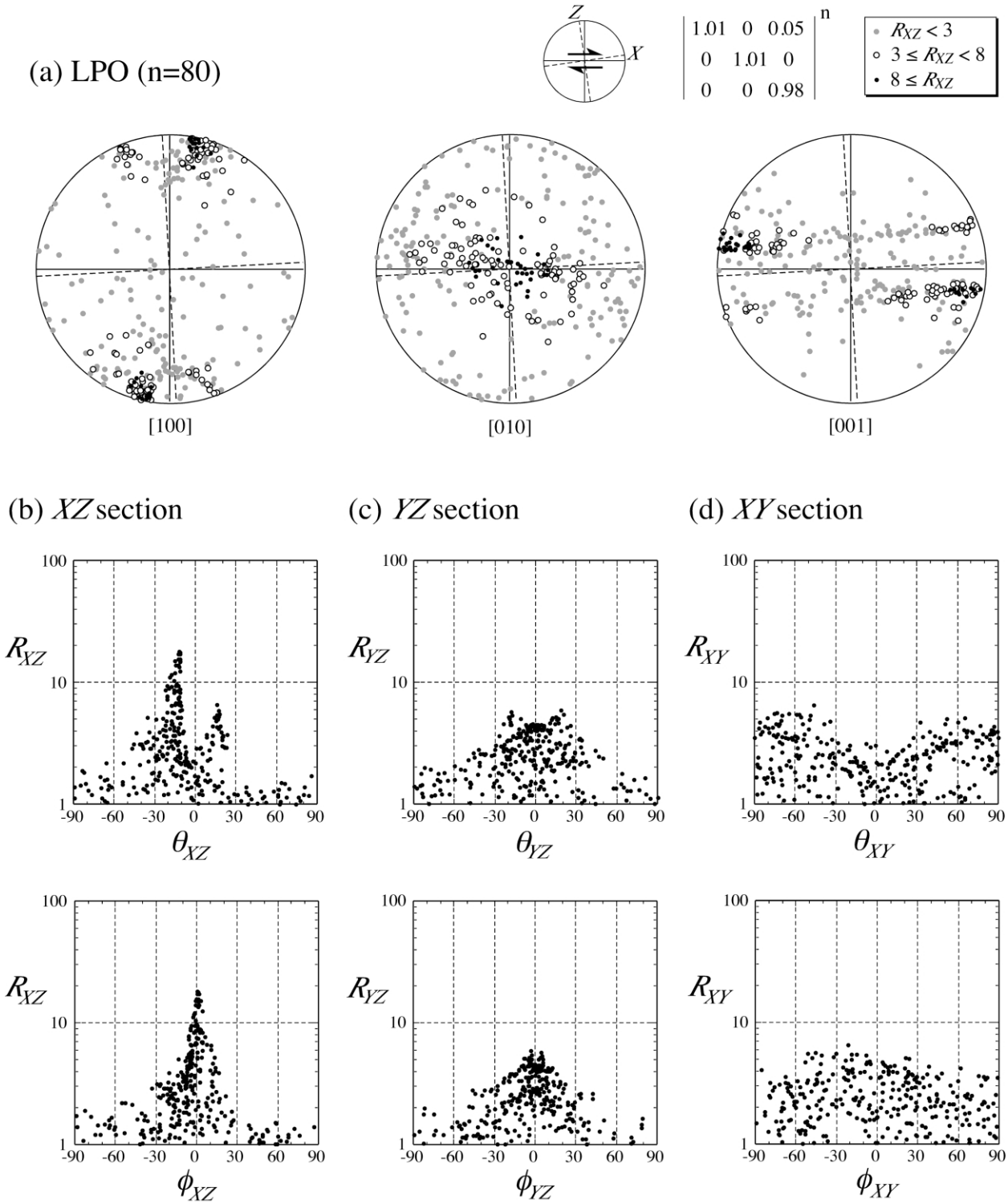

Fig. 14. LPO (a) and $R-\theta-\phi$ relations in three sections ((b)–(d)) for a matrix deformation by a combination of progressive simple shear and uniaxial shortening. The direction of uniaxial shortening is normal to the shear plane of simple shear component (coupled arrows in an inset). Axial ratio of a finite strain ellipsoid for matrix deformation is $X{:}Y{:}Z = 4.03{:}2.22{:}0.11$.

elliptical inclusions compared with that predicted by theory, but not stabilization. In contrast, interslip results in stabilization of parallelogram-shaped inclusions, with the long diagonal oriented at a small antithetic angle to the shear direction. Mancktelow et al. (2002) concluded that interface slip is one mechanism of stabilization for elongate parallelogram-shaped inclusions.

To summarize previous studies, rigid inclusions in a simple-shearing matrix have stable orientations inclined antithetically from the shear plane under several conditions

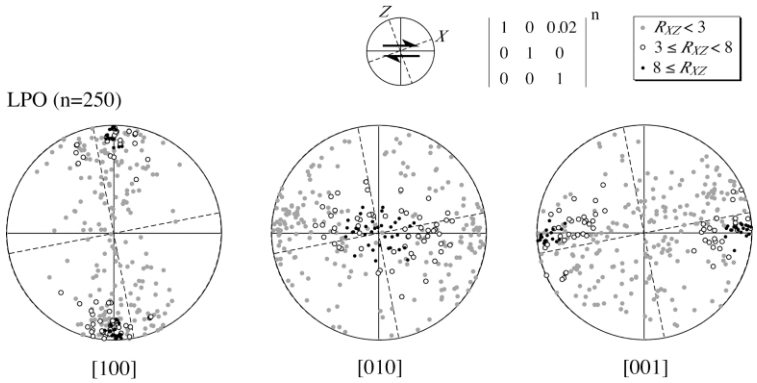

Fig. 15. LPO of initially ellipsoidal grains in a matrix deforming by progressive simple shear after deformation increments (n) of 250. Initial grain shape is d_1:d_2:d_3 = 1:2:1.4, where d_1, d_2 and d_3 indicate grain diameter parallel to [100], [010] and [001] directions, respectively. Axial ratio of a finite strain ellipsoid for matrix deformation is X:Y:Z = 5.19:1:0.19.

of combinations of non-elliptical (i.e. elongate parallelogram or rectangle) grain shape, non-Newtonian matrix rheology, and interface slip.

Orthopyroxene porphyroclasts in the present peridotite mylonite also exhibit strong SPO with long axes inclined antithetically about 10° to the shear direction (Fig. 4). This strong SPO can be simulated by the present model as the product of deformation and rigid-body rotation of orthopyroxene porphyroclasts. Therefore, deformable inclusions can be considered to be a valuable additional model for strong SPO antithetically inclined from the shear direction.

For matrix deformation by simple shear, SPO parallel to the finite strain axes of matrix deformation results in SPO antithetically inclined from the shear direction. The SPO of passive elliptical inclusions (i.e. inclusions without rheological contrast with the matrix) is also parallel to the finite strain axes of matrix deformation (e.g. Ramsay, 1967; Dunnet, 1969; Ramsay and Huber, 1983). However, there are several differences between passive inclusions and the present grain model. For a large 2D strain (i.e. $R_s > R_i$, where R_s and R_i are the axial ratio of the strain ellipse and the initial aspect ratio of inclusions), the maximum and minimum aspect ratios (R_{max} and R_{min}) of passive inclusions are $R_{max} = R_i R_s$ and $R_{min} = R_s/R_i$. This then gives the relations $R_i = \sqrt{R_{max}/R_{min}}$ and $R_s = \sqrt{R_{max}R_{min}}$. For the case of unique initial aspect ratio of inclusions, therefore, a wide range of aspect ratio of deformed inclusions implies a large initial aspect ratio of inclusions (for example $R_i = 5$ for $R_{max} = 25$ and $R_{min} = 1$). In contrast, for the present model, $R_s \approx R_{max}$ and grains with a wide range of aspect ratio are derived from initially circular grains with variable crystallographic orientation (Ishii and Sawaguchi, 2002). Although the relationship between grain shape and matrix deformation for 3D deformation is not simple, it is clear that the behavior of grains in the present model is different from that of passive ellipsoidal inclusions. These differences are ascribed to the highly anisotropic behavior of grains in the model due to the unique slip system. This indicates that the SPO of deformable inclusions is also controlled by the degree of anisotropy as well as the rheological contrast between inclusions and the matrix. As the deformational behavior of a perfectly anisotropic grain changes from passive to rigid according to its orientation, rigid, passive and anisotropic ellipsoidal inclusions are considered to be ternary end-members of the deformational conditions of inclusions.

5.5. LPO

Several simulation models for the development of the LPO of grains with unique slip system have been proposed (Etchecopar, 1977; Wenk et al., 1991; Zhang et al., 1994). Simulation results from a purely geometrical model (Etchecopar, 1977) and a model based on the finite difference method (Zhang et al., 1994) show that glide-plane orientations become separated into two orientations during progressive pure shear and simple shear and that these two orientations are oblique to the long axis of the strain ellipse. In addition, for simple shear deformation, one of the orientations is sub-parallel to the shear plane. This is consistent with the present simulation results. In contrast, simulations of peridotites (two-phase aggregates of 70% olivine–30% orthopyroxene) using viscoplastic self-consistent theory show that the [001] orientation of orthopyroxene becomes concentrated around the long axis of the strain ellipsoid for pure and simple shear deformation (Wenk et al., 1991). This difference may be ascribed to the shape-dependent rotation of grains, which may not have been taken into consideration in Wenk et al. (1991).

5.6. Implications of 3D numerical modeling

Kinematical analysis of rock deformation has advanced markedly in the last two decades (e.g. Lister and Williams, 1979, 1983; Means et al., 1980; Passchier and Simpson, 1986; Ishii, 1992, 1995; Masuda et al., 1995; see also Passchier and Trouw, 1996 for reviews). In most studies, however, rock fabrics have been analyzed in two dimensions and ductile shear zones have been assumed to develop by progressive plane-strain deformation. In a plane-strain

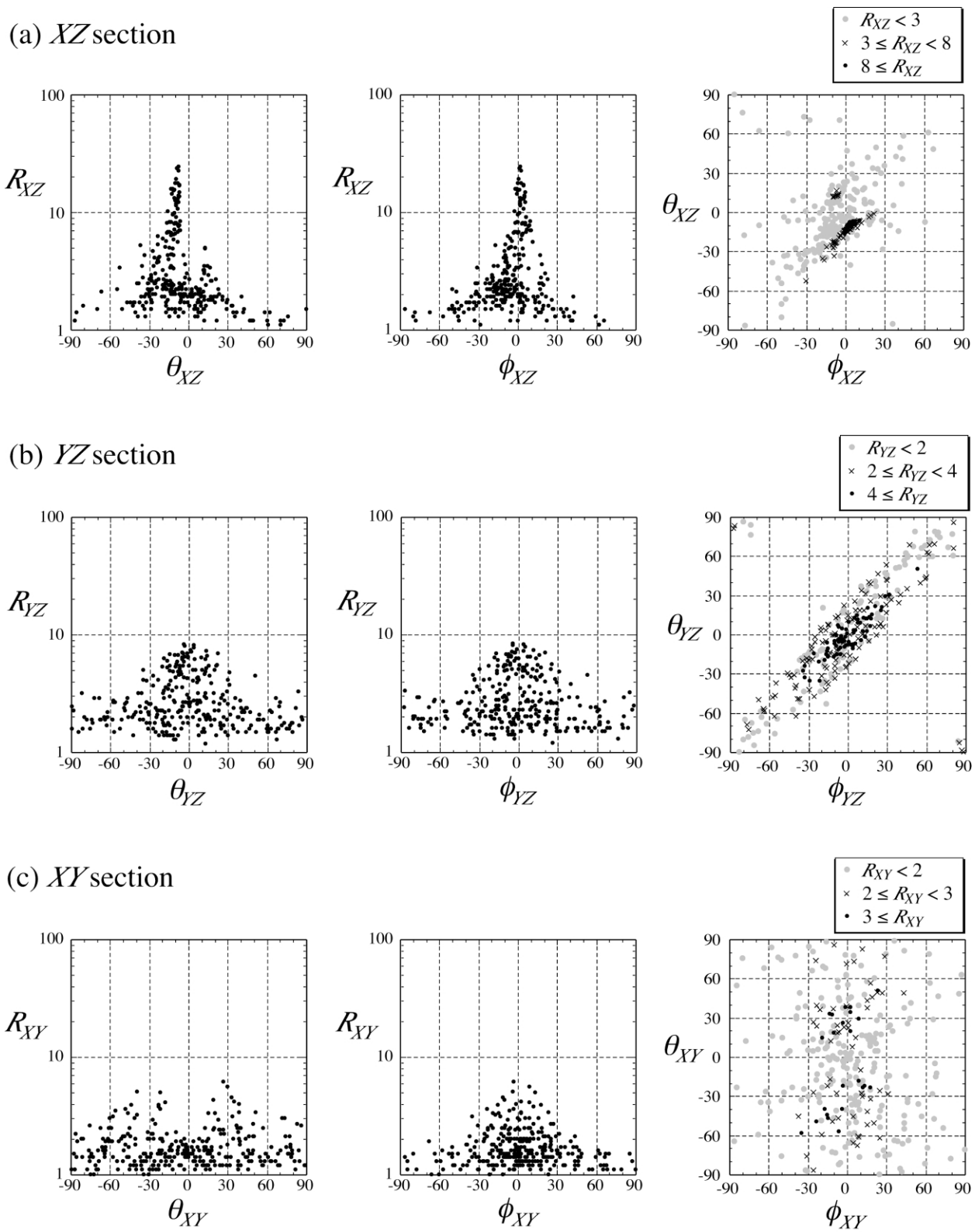

Fig. 16. $R-\theta-\phi$ relations in XZ section (a), YZ section (b) and XY section (c) after 250 deformation increments by simple shear. Initial grain shape is $d_1{:}d_2{:}d_3 = 1{:}2{:}1.4$.

shear zone, the vorticity vector should be parallel to the shear zone and perpendicular to both the finite elongation axis (lineation) and the relative displacement direction of the wall. However, several natural shear zones have been reported in which the vorticity vector is not perpendicular to the lineation or the orientation of lineation changes across the zone (e.g. Hudleston et al., 1988; Robin and Cruden, 1994; Tikoff and Greene, 1997; see also Jiang and Williams (1998) and Passchier (1998) for theoretical analysis of general shear deformation). Such 3D ductile shear zones are therefore not unusual, and independent information of finite strain geometry and orientation of the vorticity vector are indispensable for kinematical analysis of natural shear zones. The present model is able to trace the change in both crystallographic orientation and grain shape of porphyroclasts. As shown in Fig. 13, the SPO of grains has nearly axial symmetry, reflecting the geometry of the finite strain ellipsoid. On the other hand, the LPO of grains has monoclinic symmetry with clear asymmetry in the *XZ* plane, indicating that the vorticity vector is parallel to the *Y* axis. The present 3D numerical modeling approach is considered, based on comparison with natural examples, to be useful for the kinematic analysis of general shear zones.

6. Summary

A 3D numerical model for simulating the development of lattice- and shape-preferred orientation of orthopyroxene porphyroclasts in a fine-grained olivine matrix was proposed. In the model, grains are deformed by dislocation glide on a unique slip system and by rigid-body rotation. The simulation results revealed several features. Grains became separated into two groups with $\theta_{XZ} < \phi_{XZ}$ and $\theta_{XZ} > \phi_{XZ}$. The slip plane and slip direction of elongated grains were parallel to the shear plane and shear direction of simple-shearing matrix deformation. Strong SPO formed parallel to the elongation axis of matrix deformation. A natural peridotite mylonite sample also exhibited these features.

Similar to many other porphyroclasts in natural mylonitic rocks, orthopyroxene porphyroclasts in the present peridotite mylonite exhibited strong SPO with long axes inclined antithetically to the shear direction. Anisotropically deformable inclusions may be one mechanism for the development of this SPO.

The present 3D model has broader applicability than the previous 2D model, which is only applicable to plane-strain deformations. In addition, the present model is able to trace the change in both the crystallographic orientation and grain shape of porphyroclasts. Therefore, independent information of the finite strain geometry and orientation of the vorticity vector may be obtainable by application of the present model to natural shear zones.

Acknowledgements

The authors thank T. Takeshita and K. Kanagawa for critical reading and improvements of early versions of the manuscript. Gratitude is also extended to P. Bons and an anonymous referee for constructive reviews and J. Hippertt for editorial handling.

References

Arbaret, L., Diot, H., Bouchez, J.-L., 1996. Shape fabrics of particles in low concentration suspensions: 2D analogue experiments and application to tiling in magma. Journal of Structural Geology 18, 941–950.

Bilby, B.A., Eshelby, J.D., Kundu, A.K., 1975. The changes in shape of a viscous ellipsoidal region embedded in a slowly deforming matrix having a different viscosity. Tectonophysics 28, 265–274.

Darot, M., Boudier, F., 1975. Mineral lineations in deformed peridotites: kinematic meaning. Petrologie 1, 225–236.

Dornbusch, H.-J., Weber, K., Skrotzki, W., 1994. Development of microstructure and texture in high-temperature mylonites from the Ivrea Zone. In: Bung, H.J., Siegesmund, S., Skrotzki, W., Weber, K. (Eds.), Textures of Geological Materials, DGM Informationsgesellschaft, Oberursel, pp. 187–201.

Dunnet, D., 1969. A technique of finite strain analysis using elliptical particles. Tectonophysics 7, 117–136.

Eshelby, J.D., 1957. The determination of the elastic field of an ellipsoidal inclusion, and related problems. Proceedings of the Royal Society of London, Series A 241, 376–396.

Etchecopar, A., 1977. A plane kinematic model of progressive deformation in a polycrystalline aggregate. Tectonophysics 39, 121–139.

Etchecopar, A., Vasseur, G., 1987. A 3-D kinematic model of fabric development in polycrystalline aggregates: comparisons with experimental and natural examples. Journal of Structural Geology 9, 705–717.

Freeman, B., 1985. The motion of rigid ellipsoidal particles in slow flows. Tectonophysics 113, 163–183.

Freeman, B., 1987. The behaviour of deformable ellipsoidal particles in three-dimensional slow flows: implications for geological strain analysis. Tectonophysics 132, 297–309.

Gay, N.C., 1968. The motion of rigid particles embedded in a viscous fluid during pure shear deformation of the fluid. Tectonophysics 5, 81–88.

Ghosh, S.K., Ramberg, H., 1976. Reorientation of inclusions by combinations of pure and simple shear. Tectonophysics 34, 1–70.

ten Grotenhuis, S.M., Passchier, C.W., Bons, P.D., 2002. The influence of strain localisation on the rotation behaviour of rigid objects in experimental shear zones. Journal of Structural Geology 24, 485–499.

Hanmer, S., 2000. Matrix mosaics, brittle deformation, and elongate porphyroclasts: granulite facies microstructures in the Striding–Athabasca mylonite zone, western Canada. Journal of Structural Geology 22, 947–967.

Hinch, E.J., Leal, L.G., 1979. Rotation of small non-axisymmetric particles in simple shear flow. Journal of Fluid Mechanics 92, 591–608.

Hudleston, P.J., Schultz-Ela, D., Southwick, D.L., 1988. Transpression in an Archean greenstone belt, northern Minnesota. Canadian Journal of Earth Science 25, 1060–1068.

Ildefonse, B., Mancktelow, N.S., 1993. Deformation around rigid particles: the influence of slip at the particle/matrix interface. Tectonophysics 221, 345–359.

Ildefonse, B., Launeau, P., Bouchez, J.-L., Fernandez, A., 1992a. Effect of mechanical interactions on the development of shape preferred orientations: a two-dimensional experimental approach. Journal of Structural Geology 14, 73–83.

Ildefonse, B., Sokoutis, D., Mancktelow, N.S., 1992b. Mechanical

interactions between rigid particles in a deforming ductile matrix. Analogue experiments in simple shear flow. Journal of Structural Geology 14, 1253–1266.

Ishii, K., 1992. Partitioning of non-coaxiality in deforming layered rock masses. Tectonophysics 210, 33–43.

Ishii, K., 1995. Estimation of non-coaxiality from crinoid-type pressure fringes: comparison between natural and simulated examples. Journal of Structural Geology 17, 1267–1278.

Ishii, K., Sawaguchi, T., 2002. Lattice- and shape-preferred orientation of orthopyroxene porphyroclasts in peridotites: an application of two-dimensional numerical modeling. Journal of Structural Geology 24, 517–530.

Jeffery, G.B., 1922. The motion of ellipsoidal particles immersed in a viscous fluid. Proceedings of the Royal Society of London, Series A 102, 161–179.

Jezek, J., Melka, R., Schulmann, K., Venera, Z., 1994. The behaviour of rigid triaxial ellipsoidal particles in viscous flows—modeling of fabric evolution in a multiparticle system. Tectonophysics 229, 165–180.

Jezek, J., Schulmann, K., Segeth, K., 1996. Fabric evolution of rigid inclusions during mixed coaxial and simple shear flows. Tectonophysics 229, 165–180.

Jiang, D., Williams, P.F., 1998. High-strain zones: a unified model. Journal of Structural Geology 20, 1105–1120.

Komatsu, M., Osanai, Y., Toyoshima, T., Miyashita, S., 1989. Evolution of the Hidaka metamorphic belt, northern Japan. Journal of the Geological Society of London, Special Publication 43, 487–493.

Lister, G.S., Hobbs, B.E., 1980. The simulation of fabric development during plastic deformation and its application to quartzite: the influence of deformation history. Journal of Structural Geology 2, 355–370.

Lister, G.S., Paterson, M.S., 1979. The simulation of fabric development during plastic deformation and its application to quartzite: fabric transitions. Journal of Structural Geology 1, 99–115.

Lister, G.S., Snoke, A.W., 1984. S–C mylonites. Journal of Structural Geology 6, 617–638.

Lister, G.S., Williams, P.F., 1979. Fabric development in shear zones: theoretical controls and observed phenomena. Journal of Structural Geology 1, 283–297.

Lister, G.S., Williams, P.F., 1983. The partitioning of deformation in flowing rock masses. Tectonophysics 92, 1–33.

Lister, G.S., Paterson, M.S., Hobbs, B.E., 1978. The simulation of fabric development during plastic deformation and its application to quartzite: the model. Tectonophysics 45, 107–158.

Mancktelow, N.S., Arbaret, L., Pennacchioni, G., 2002. Experimental observations on the effect of interface slip on rotation and stabilisation of rigid particles in simple shear and a comparison with natural mylonites. Journal of Structural Geology 24, 567–585.

Marques, F.O., Coelho, S., 2001. Rotation of rigid elliptical cylinders in viscous simple shear flow: analogue experiments. Journal of Structural Geology 23, 609–617.

Masuda, T., Michibayashi, K., Ohta, H., 1995. Shape preferred orientation of rigid particles in a viscous matrix: re-evaluation to determine kinematic parameters of ductile deformation. Journal of Structural Geology 17, 115–129.

Means, W.D., Hobbs, B.E., Lister, G.S., Williams, P.F., 1980. Vorticity and non-coaxiality in progressive deformations. Journal of Structural Geology 2, 371–378.

Mercier, J.-C. C., 1985. Olivine and pyroxenes. In: Wenk, H.-R., (Ed.), Preferred Orientation in Deformed Metals and Rocks: An Introduction to Modern Texture Analysis, Academic Press, Orlando, pp. 407–430.

Molinari, A., Canova, G.R., Ahzi, S., 1987. A self-consistent approach of the large deformation polycrystal viscoplasticity. Acta Metallurgica 35, 2983–2994.

Niida, K., 1974. Structure of the Horoman ultramafic mass of the Hidaka metamorphic belt in Hokkaido, Japan. The Journal of the Geological Society of Japan 80, 31–44.

Niida, K., 1975. Texture of olivine fabrics and the Horoman ultramafic rocks, Japan. Journal of Mineralogy, Petrology and Economic Geology 70, 265–285.

Niida, K., 1984. Petrology of the Horoman ultramafic rocks. Journal of the Faculty of Science, Hokkaido University, Series IV 21, 61–81.

Obata, M., Nagahara, N., 1987. Layering of alpine-type peridotite and the segregation of partial melt in the upper mantle. Journal of Geophysical Research 92, 3467–3474.

Osanai, Y., Owada, M., Kawasaki, T., 1992. Tertiary deep crustal ultrametamorphism in the Hidaka metamorphic belt, northern Japan. Journal of Metamorphic Geology 10, 401–414.

Ozawa, K., Takahashi, N., 1995. P–T history of a mantle diapir: the Horoman peridotite complex, Hokkaido, northern Japan. Contributions to Mineralogy and Petrology 120, 223–248.

Passchier, C.W., 1987. Stable positions of rigid objects in non-coaxial flow—a study in vorticity analysis. Journal of Structural Geology 9, 679–690.

Passchier, C.W., 1998. Monoclinic model shear zones. Journal of Structural Geology 20, 1121–1137.

Passchier, C.W., Simpson, C., 1986. Porphyroclast systems as kinematic indicators. Journal of Structural Geology 8, 831–843.

Passchier, C.W., Trouw, R.A.J., 1996. Microtectonics, Springer-Verlag, Berlin.

Pennacchioni, G., Toro, G.D., Mancktelow, N.S., 2001. Strain-insensitive preferred orientation of porphyroclasts in Mont Mary mylonites. Journal of Structural Geology 23, 1281–1298.

Ramsay, J.G., 1967. Folding and Fracturing of Rocks, McGraw-Hill, New York.

Ramsay, J.G., Huber, H.I., 1983. The Techniques of Modern Structural Geology. Volume 1: Strain Analysis, Academic Press, London.

Reed, L.J., Tryggvason, E., 1974. Preferred orientation of rigid particles in a viscous matrix deformed by pure shear and simple shear. Tectonophysics 24, 85–98.

Reuber, I., Michard, A., Chalouan, A., Juteau, T., Jermoumi, B., 1982. Structure and emplacement of the Alpine-type peridotites from Beni Bousera, Rif, Morocco: a polyphase tectonic interpretation. Tectonophysics 82, 231–251.

Robin, P.-Y.F., Cruden, A.R., 1994. Strain and vorticity patterns in ideally ductile transpression zones. Journal of Structural Geology 16, 447–466.

Sawaguchi, T., Takagi, H., 1997. Inverted ductile shear movement of the Horoman peridotite complex in the Hidaka metamorphic belt, Hokkaido, Japan. The Memoirs of the Geological Society of Japan 47, 193–208.

Sawaguchi, T., Goto, K., Takagi, H., 2001. Elongated orthopyroxene porphyroclast as a shear sense indicator and kinematic history of the Horoman Peridotite Complex, Hokkaido, Japan. The Journal of the Geological Society of Japan 107, 165–178.

Suhr, G., 1993. Evaluation of upper mantle microstructures in the Table Mountain massif (Bay of Islands ophiolite). Journal of Structural Geology 15, 1273–1292.

Takahashi, N., 1991. Origin of three peridotite suites from Horoman peridotite complex, Hokkaido Japan; melt segregation and solidification process in the upper mantle. Journal of Mineralogy, Petrology and Economic Geology 86, 199–215.

Takahashi, N., 1992. Evidence for melt segregation toward features in the Horoman mantle peridotite complex. Nature 359, 52–55.

Takazawa, E., Frey, F.A., Obata, M., Bodinier, J.L., 1992. Geochemical evidence for melt migration and reaction in the upper mantle. Nature 359, 55–58.

Takazawa, E., Frey, F.A., Shimizu, N., Obata, M., 1996. Evolution of the Horoman peridotite: implications from pyroxene compositions. Chemical Geology 134, 3–26.

Takazawa, E., Frey, F.A., Shimizu, N., Saal, A., Obata, M., 1999. Polybaric petrogenesis of mafic layers in the Horoman Peridotite Complex, Japan. Journal of Petrology 40, 1827–1851.

Takazawa, E., Frey, F.A., Shimizu, N., Obata, M., 2000. Whole rock compositional variations in an upper mantle peridotite (Horoman,

Hokkaido, Japan): are they consistent with a partial melting process? Geochimica et Cosmochimica Acta 64, 695–716.

Takeshita, T., Wenk, H.-R., Molinari, A., Canova, G.R., 1990. Simulation of dislocation-assisted plastic deformation in olivine polycrystals. In: Barber, D.J., Meredith, P.G. (Eds.), Deformation Mechanisms in Minerals, Ceramics and Rocks, Unwin Hyman Ltd, London, pp. 365–376.

Tikoff, B., Greene, D., 1997. Stretching lineations in transpressional shear zones: an example from the Sierra Nevada batholith, California. Journal of Structural Geology 19, 29–39.

Tikoff, B., Teyssier, C., 1994. Strain and fabric analyses based on porphyroclast interaction. Journal of Structural Geology 16, 477–491.

Toyoshima, T., 1998. Gabbro mylonite developed along a crustal-scale décollement. In: Snoke, A.W., Tullis, J., Todd, V.R. (Eds.), Fault-related Rocks: A Photographic Atlas, Princeton University Press, Princeton, pp. 426–427.

Tubía, J.M., 1994. The Ronda peridotites (Los Reales nappe): an example of the relationship between lithospheric thickening by oblique tectonics and late extensional deformation within the Betic Cordillera (Spain). Tectonophysics 238, 381–398.

Wenk, H.-R., Canova, G., Molinari, A., Kocks, U.F., 1989. Viscoplastic modeling of texture development in quartzite. Journal of Geophysical Research 94, 17895–17906.

Wenk, H.-R., Bennett, K., Canova, G., Molinari, A., 1991. Modeling plastic deformation of peridotite with the self-consistent theory. Journal of Geophysical Research 96, 8337–8349.

Zhang, Y., Wilson, C.J.L., 1997. Lattice rotation in polycrystalline aggregates and single crystals with one slip system: a numerical and experimental approach. Journal of Structural Geology 19, 875–885.

Zhang, Y., Hobbs, B.E., Ord, A., 1994. A numerical simulation of fabric development in polycrystalline aggregates with one slip system. Journal of Structural Geology 16, 1297–1313.